Research Article | Vol. 29, No. 13 / 21 June 2021 / Optics Express 19417
Optics EXPRESS

Dynamic reflective color pixels based on molybdenum oxide

G. Santos,[1] F. Gonzalez,[1] D. Ortiz,[1] J. M. Saiz,[1] M. Losurdo,[2] F. Moreno,[1] and Y. Gutierrez[2,*]

[1]Group of Optics, Department of Applied Physics Faculty of Sciences, University of Cantabria, Spain
[2]Institute of Nanotechnology CNR-NANOTEC, Via Orabona 4, 70126 Bari, Italy
[*]yael.gutierrezvela@nanotec.cnr.it

Abstract: Active materials which show phase transitions, usually known as Phase Change Materials (PCM), have paved the way to a new generation of reconfigurable plasmonic platforms. Tunable color devices have experienced a great development in the recent years. In particular, reflective color filters can take advantage from sunlight to select and reflect a specific resonant wavelength in the visible spectrum range. Reflective displays are usually structural color filters based on asymmetric Fabry-Perot cavities (AFPCs). For a fixed geometry, most of AFPCs filters generate static color, limiting their potential as tunable color devices. Dynamic color is achieved by introducing an active layer whose optical properties can be modulated by an external stimuli. In this paper, we propose AFPCs based on molybdenum oxide (MoO_x, $2<x<3$) to achieve switchable *on*/*off* color reflective pixels. *On* and *off* states of the pixels are controlled through the stoichiometry of the MoO_x layer.

1. Introduction

Structural color filtering has emerged as an attractive alternative to chemical color. Although pigments and dyes allow a wide viewing angle and high contrast ratio, their performance is limited by the degradation produced by long-time illumination [1] and the fact that most of them are not environmentally friendly [2]. Therefore, structural color has gained extensive attention because of the wide range of possible applications such as color decoration, imaging sensing, printing and optical imaging among others [3–9]. The most important aspects that must be verified by structural color strategies for their successful applicability in the aforementioned fields are: a wide color gamut, large viewing angle and scalable fabrication.

Color reflective displays are structural color filters usually based on plasmonic nanostructures [10–15] and/or asymmetric Fabry-Perot cavities (AFPCs). Surrounding light is used as a source, from which specific wavelength intervals within the visible spectrum are reflected. Color can be tuned modifying light source, polarization, incidence angle and the material and geometry of the cavities which compose the reflective display. CMY (cyan-magenta-yellow) substractive colors present higher reflectivity than RGB (red-green-blue) color system [16], so that CMY reflective subpixels allow the generation of an efficient gamut color device. Reflective subpixels can be considered the most efficient configuration for many situations as they can provide color with good visibility and without power consumption. By contrast, emissive displays, such as LED and OLED, need to increase power intensity to guarantee good outdoor visibility [17].

There are several studies proposing different designs of AFPCs reflective color filters [18–22]. One of the most common configurations consists on a metal-insulator-metal (MIM) structure. This configuration is composed by a thin metal layer to control the spectral bandwidth of the reflectance peaks, a dielectric spacer to tune the resonant wavelength in the cavity and a second metal layer that works as a mirror to reflect the incident light. However, most of the proposed MIM color filters generate static color for a fixed geometry, limiting their potential as actively tunable color devices. One way of solving this consists in introducing an active layer which

#424763 https://doi.org/10.1364/OE.424763
Journal © 2021 Received 11 Mar 2021; revised 3 May 2021; accepted 18 May 2021; published 8 Jun 2021

Optics EXPRESS

usually is made of a phase-change material (PCM). The peculiarity of these materials is that they can be switched between their crystalline and amorphous phases by either controlled electrical, optical or thermal excitation [23]. This process leads to a modulation of their optical and electrical properties without requiring a energy supply to maintain the switched state. Is this controlled modulation of the optical properties through external stimuli which has been introduced as an innovative element in AFPCs to create dynamic color pixels. The most known PCMs are the GST-family due to the chalcogenide $Ge_2Sb_2Te_5$, which has revolutionized the blooming field of phase-change photonics. For instance, very recent studies have proposed a ITO/GST/ITO/Pt design, where GST acts as the active layer that allows the modulation of the reflective color [24–28]. Other authors have proposed the use of GeTe as active element in this type of AFPC structure [29].

In this paper, we propose reconfigurable AFPCs whose active layer is based on molybdenum oxides (MoO_x, $2<x<3$) in order to achieve a switchable *on*/*off* color display. Molybdenum oxide can exist as semi-metallic MoO_2, wide band gap MoO_3 and in a wide range of stoichiometries MoO_x with $2<x<3$ (i.e. $Mo_{18}O_{52}$, $Mo_{17}O_{47}$, Mo_9O_{26}, Mo_8O_{23}, Mo_5O_{14} and Mo_4O_{11}). The change in the oxygen content strongly affects its band structure and, consequently, its optical behavior. In our proposed reflective display configuration, MoO_3 acts as a loss-less transparent dielectric in the visible ($E_{gap} \approx 3$ eV depending on the crystallinity [30]), allowing the production and modulation of vivid colors inside the AFPCs (*on* mode). On the contrary, MoO_2 absorbs the visible light and a constant dull color is reflected (*off* mode). Molybdenum oxides can be considered a non volatile material, i.e., it does not require a constant energy supply of energy to keep the switched state. Interestingly, the intervalence charge-transfer modulation within diverse valence state of Mo, going from Mo^{6+} (MoO_3), to Mo^{5+} and finally to Mo^{4+} (MoO_2), i.e., the MoO_3/MoO_2 phase transition, can be switched thermally by annealing at 400°C in air or hydrogen, involving the thermal activated adsorption/desorption of oxygen according to reactions,

$$2MoO_2 + O_2 \rightarrow 2MoO_3$$

or

$$MoO_3 + H_2 \rightarrow MoO_2 + H_2O$$

Noteworthy, this innovative way of modulating the annealing and therefore the oxygen content and phase transition in oxides has been recently reported for the PCM VO_2 [31].

Those annealing and phase transitions can be operated starting from deposited MoO_3 or MoO_2; that can be obtained by (*i*) controlling the stoichiometry during the growth by the oxygen partial pressure, or (*ii*) by post growth processing which includes ion bombardment, which results in the preferential loss of bridging oxygen atoms and oxygen plasmas.

2. Device design and working principle

2.1. Layer geometry

The designed reflective display structures are based on asymmetric Fabry-Perot cavities (AFPCs) as the one shown in Fig. 1. A multi-layer film stack composed of indium tin oxide (ITO)/ molybdenum oxide (MoO_x)/ ITO / platinum (Pt). The first ITO layer thickness is fixed to 20 nm and the Pt layer is thick enough as to be considered a semi-infinite medium (substrate). The thicknesses of the second ITO layer (spacer) and the MoO_x layer have been varied for the optimization of the device.

Each material and layer plays a different role. The Pt substrate is a good choice for the mirror due to its high melting point (1768°C) and environmental stability. Moreover, Pt is compatible with the integration of a microheater into the bottom of the mirror for each pixel [29]. The active element, MoO_x, is a material whose carrier density can be modulated by adjusting its oxygen content. The change in stoichiometry, x, affects its optical response. In MoO_3, O_{2p} orbitals

Optics EXPRESS

give rise to the highest occupied states wherein electrons are fully localized around the O atoms leading to a semiconducting behavior. However, the Fermi level of MoO_2 is composed of Mo_{3d} orbitals that show metallic behaviour. Moreover, calculations of electron localization functions have shown that the free electron gas density is higher for MoO_2 than for MoO_3 [32]. Therefore, by switching from MoO_3 to MoO_2, a semiconductor - conductor transition is triggered, giving rise to a modulation of the light-matter interaction [33]. In this design, two measurements of oxygen contents are considered: x=2.9 (*on*) and x=2.1 (*off*). In the *on* state light can travel trough it, allowing Fabry-Perot reflection resonances which in turn produce vivid colors. However in the *off* state most of the light is absorbed, resonances are not produced and a pale unsaturated color is reflected.

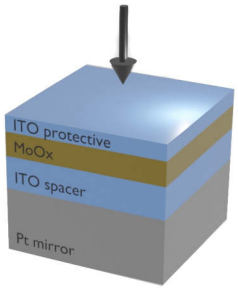

Fig. 1. Schematic structure of the designed reflective display based on an asymmetric Fabry-Perot cavity made of a mutilayer film whose elements are ITO/MoO_x/ITO spacer/Pt.

Indium tin oxide (ITO) is a transparent conductive oxide. It was chosen to be at the top of the stack to protect MoO_x from the environment attack. In addition, it is proposed to act as a spacer between the MoO_x and Pt layers. The thickness of the ITO spacer layer can be used as a tuning element of the resonant wavelength in the cavity, and thus, of the reflective color. Given the high electrical conductivity of ITO, it can be used to apply a local voltage bias between the ITO spacer and a AFM cantilever while producing Joule heating locally in each pixel to activate the phase transition of MoO_x [25]. However, the main goal of ITO is wrapping MoO_x to control the oxygen content of the MoO_x layer. The refractive index of molybdenum oxide for both oxygen contents is shown in Figs. 2(a) and 2(b). The imaginary part of the refractive index k is almost zero in the *on* mode and greater than one in the *off* state.

The color reflective pixel can be considered as a FP interferometer. The light undergoes multiple reflections within the cavity. When the optical path difference between two reflected rays verifies either

$$2ndcos\theta = (2m+1)\frac{\lambda}{2} \tag{1}$$

or

$$2ndcos\theta = m\lambda \tag{2}$$

constructive or destructive interference takes place, respectively. In both equations, θ is the incident angle, n is the complex refractive index of the cavity, d its thickness, λ is the incident wavelength and m is the resonance order ($m = 0, 1, 2\cdots$). Constructive interference corresponds to reflectance maxima and destructive interference to reflectance minima. An example of interference pattern generated by the display has been simulated considering the refractive index of MoO_x x=2.9 (Fig. 2(c)) and x = 2.1 (Fig. 2(d)). In these simulations, reflectivity in 2D is represented as a function of the incident angle, for a ITO spacer and MoO_x thickness d=3μm and a wavelength λ=482nm. Each ring is associated with a different resonance order m. When the display is switched to the *off* mode, interference cannot be produced due to absorption predominance.

Optics EXPRESS

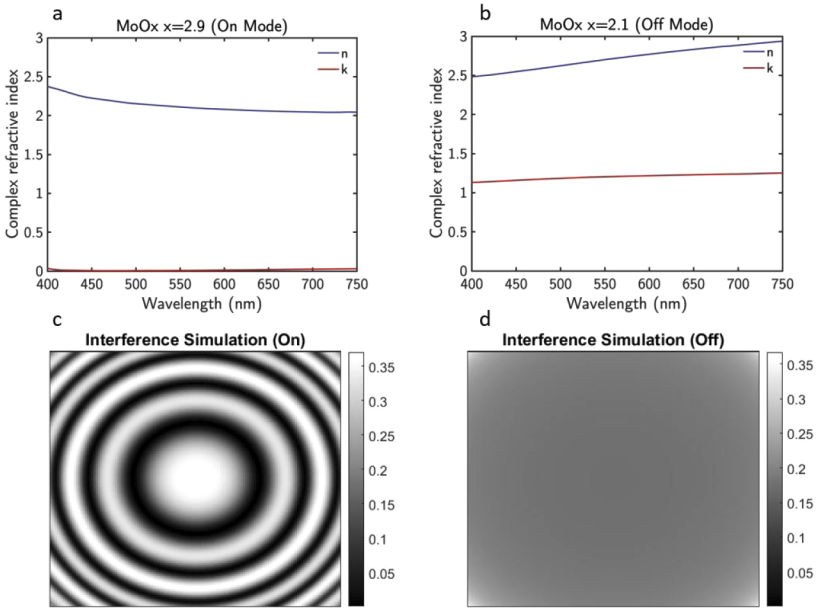

Fig. 2. Complex refractive index for x=2.9 (a) and x=2.1 (b) as a function of the wavelength (nm). (c) and (d) represent the interference patterns of the reflected radiation in a AFPC made of a ITO spacer and a MoO_x film of thickness d=3 μm for x=2.9 and x=2.1, respectively. The incident wavelength is 482 nm.

2.2. Reflectance and colorimetry

The reflectance of the multilayer structure was calculated using the Transfer Matrix Method (TMM). TMM allows to calculate the reflectance spectrum of an arbitrary system of homogeneous and non-magnetic multilayers by establishing conditions for the electric field along the boundary of two consecutive media [34,35].

The resulting color depends on spectral reflectivity, illuminant and observer. All the color simulations in this research assume standard D65 illuminant and a CIE standard observer. Illuminant D65 corresponds to average daylight, and CIE standard observer represents mean human spectral sensitivity to visible spectrum range. [36,37]. In this paper, *CIE*1931 space has been chosen because is one of the most accepted to study the resulting color by these reflective displays. Each color is represented by its chromaticity coordinates (x,y,z). The difference ΔE between two of them can be expressed as

$$\Delta E = \sqrt{(x_1 - x_2)^2 + (y_1 - y_2)^2 + (z_1 - z_2)^2} \tag{3}$$

CMY color system is often beneficial because it increases the overall reflectivity (R=M+Y, G=C+Y, B=C+M). To generate red, green or blue in the substractive color system, two of the three subpixels are mixed. This means that higher amount of light is reflected compared to RGB system where just one subpixel would reflect incident light. Therefore, mixing CMY reflective subpixels can provide a wide color gamut device with a higher luminosity.

The reflective color depends on ITO spacer and MoO_x thicknesses and in the amount of oxygen content x in the molybdenum oxide layer. Figure 3 shows the resulting collection of reflective colors that can be generated by modifying the MoO_x layer thicknesses from 20 to 200 nm and the ITO spacer thickness from 20 to 300 nm, at normal incidence and with non-polarized light. For each MoO_x thickness, the generated color for x = 2.9 (left, *on* mode) and for x = 2.1 (right, *off*

Optics EXPRESS

mode) is shown. In this way, the change in color for each state, as well as the contrast between *on* and *off* modes can be observed simultaneously for all the analyzed configurations. Thicknesses from 20 nm have been considered to use the bulk dielectric function of these materials.

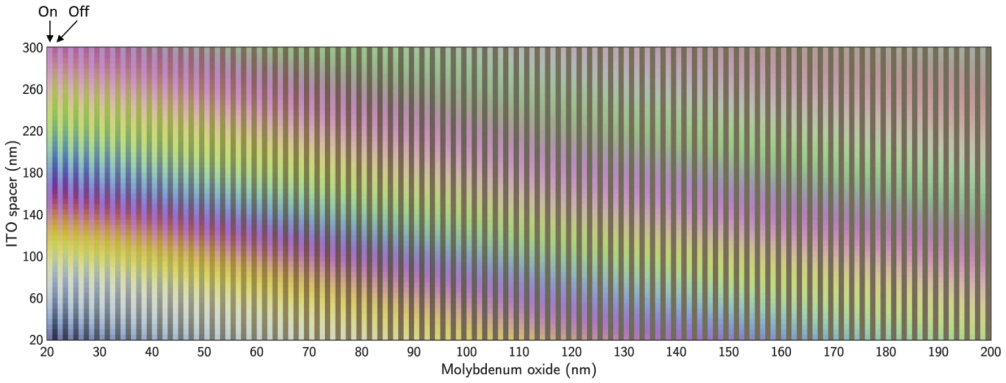

Fig. 3. Simulation of colors than can be achieved with the designed reflective display ITO/MoO_x/ITO/Pt (normal incidence and non polarized light) for MoO_x thicknesses from 20 to 200 nm and ITO spacer thicknesses from 20 to 300 nm. Each MoO_x thickness point shows the reflected color for $x = 2.9$ (left) and for $x = 2.1$ (right) case. For x=2.9 (*on* mode) a colored line can be observed whose color changes as a function of the ITO spacer thickness. For x=2.1 (*off* mode) a uniform line can be seen since there is no dominant color due to the high absorptivity in the active layer. This pale color is more notorious as the MoO_x thickness is increased.

2.3. Optimization algorithm

The main challenge is to find thicknesses of both ITO spacer and MoO_x layer from Fig. 3 that simultaneously generate the best CMY for the *on* mode and a similar color for their complementary *off* mode colors. An example of this goal is represented in Fig. 4(a). In this diagram, the vertices of the triangle represent the CMY standard coordinates. White points represent *on* colors and should be close to those vertices. Conversely, black points (*off* colors) should be far from them and close to each other revealing a constant and similar generated color. Dashed lines joint the CMY *on* states with their corresponding *off* modes.

Different magnitudes are represented in Fig. 4(a). ΔE_C, ΔE_M and ΔE_Y correspond to the color difference between *on* states and standard CMY coordinates by applying Eq. (3). ΔE_{CM}, ΔE_{MY} and ΔE_{CY} correspond to the color difference between the *off* modes (cyan-magenta, magenta-yellow and cyan-yellow *off* states, respectively). $\langle \Delta E_{on} \rangle$ and $\langle \Delta E_{off} \rangle$ can be defined as the mean color differences for the *on* and *off* states. They can be expressed as

$$\langle \Delta E_{on} \rangle = \frac{\Delta E_C + \Delta E_M + \Delta E_Y}{3} \tag{4}$$

$$\langle \Delta E_{off} \rangle = \frac{\Delta E_{CM} + \Delta E_{MY} + \Delta E_{CY}}{3} \tag{5}$$

Both magnitudes can be used to measure the quality of the two states. The ideal thicknesses would be the ones that make minimum both $\langle \Delta E_{on} \rangle$ and $\langle \Delta E_{off} \rangle$. That would means that "good" CMY colors in the *on* mode and a constant color in the *off* mode have been achieved. To make this election, an optimization algorithm has been created. The first step consists in making 3 sort lists of the 100 coupled thickness of MoO_x and ITO from Fig. 3 that makes minimum ΔE_C, ΔE_M and ΔE_Y respectively. This means that 100^3 possible configurations can be studied

Optics EXPRESS

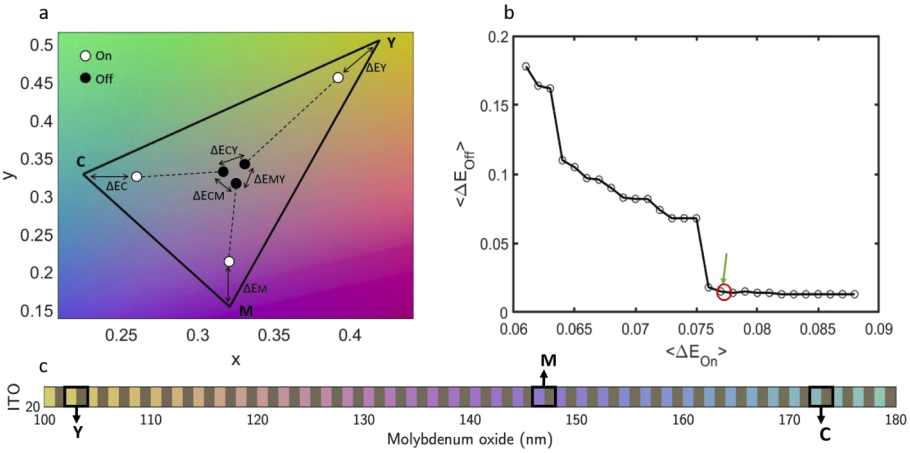

Fig. 4. (a) Chromaticity diagram where standard CMY coordinates (triangle vertices) and theoretical *on* (white points) and *off* (black points) colors are represented. (b) $\langle \Delta E_{off} \rangle$ as a function of $\langle \Delta E_{on} \rangle$ for the selected thicknesses by the algorithm. (c) Representation of the thicknesses chosen by the algorithm to generate suitable CMY *on* colors and a similar pale color in the *off* mode.

in terms of $\langle \Delta E_{on} \rangle$. To reduce this point cloud, the algorithm selects those points that makes minimum $\langle \Delta E_{off} \rangle$. The resulting points are plotted in Fig. 4(b). A decreasing tendency can be appreciated. The thicknesses that works better to create a CMY *on* state is the worse when it comes to generating the *off* mode. An equilibrium between both magnitudes should be addressed. To tackle this issue, the selected point by the algorithm is the one rounded in red. The thicknesses of both ITO and MoO_x layers that generate the selected point are shown in Table 1 and represented in Fig. 4(c).

Table 1. MoO_x and ITO thicknesses that generate the optimized cyan (C), magenta (M) and yellow (Y).

Color	MoO_x thickness (nm)	ITO thickness (nm)
C	172	20
M	146	20
Y	102	20

The ITO thicknesses is the same for the 3 cases and fits the minimum thickness imposed by the algorithm (20 *nm*). Both thicknesses can be modified to tune the resonant wavelength in the *on* state, and consequently, the reflective color. As they are increased, a spectral redshift in the visible range and a larger number of modes are obtained. It can be considered that both MoO_x and ITO spacer layers form a single effective medium. So, when one of their thicknesses increases, the other should be reduced in order to guarantee interference condition. Therefore, it is better to fix ITO spacer to 20 nm and increase MoO_x layer to absorb more amount of light and consequently, to generate the most pale color in the *off* state.

3. Results

The CMY colors obtained after the optimization of the MoO_x and ITO spacer layers in the proposed multilayered structure are shown in Fig. 5(a). The optimized CMY colors for *on* mode are plotted (left) along with the uniform flat colors generated in the *off* mode (center) and the standard CMY (right). Figure 5(b) shows the representation of these colors in the chromaticity

Optics EXPRESS

diagram. White points (*on* colors) are close to standard CMY coordinates. Black points (*off* colors) are far from them and close to each other bringing out a similar generated color.

Reflected colors are the result of constructive interference at specific wavelengths. Cyan is generated by a resonant wavelength between 485 and 500 nm. Magenta is an hybrid of red (625-740 nm) and blue (450-485 nm) modes. Yellow reflectance peak is generated between 565 and 590 nm. The spectral reflectivity of the generated CMY colors, i.e, for the thicknesses in Table 1, are shown in Figs. 5(c) and 5(d) for the *on* and *off* modes, respectively. The CMY resonant wavelengths are represented by dashed lines in Fig. 5(c) and are shown in Table 2.

Table 2. Resonant wavelengths for cyan (C), magenta (M) and yellow (Y).

Color	Resonant Wavelength (nm)
C	485
M	442 (B) + 740 (R)
Y	608

Figure 5(d) shows very flat reflectivity curves in all the visible spectrum range for the three *off* modes due to the high absorption of molybdenum oxide. This is the reason for a similar pale reflected color. In contrast, in Fig. 5(c), CMY resonances wavelengths generate reflective peaks and consequently, vivid colors can be reflected. The spectral bandwidth was larger for the red and yellow modes (long wavelengths) because its Fabry-Perot resonances are of first order. In contrast, cyan and blue modes (short wavelengths) correspond to resonances of second order. The higher the order, the narrower the bandwidth. Therefore, the use of higher resonance orders is favorable in terms of color gamut to obtain monochromatic colors. However, when the resonance order is high, the distance between different resonances decreases, leading to undesirable peaks in the visible spectrum range.

All the above color simulations have been calculated at normal incidence. The real situation is that the display receives surrounding light at different incident angles, so reflectivity shows angular dependence, and consequently, reflected color may show differences for every viewing angle. In order to assess the importance of this issue, Figs. 5(e) and 5(f) shows respectively, the reflective color of the *on* and *off* modes for different incident angles.

In the *Lab* space, color difference is perceptible for a common human eye when $\Delta E > 2$ [38]. In *CIE*1931 space, a threshold ΔE cannot be defined due to the absence of a linear relationship between chromaticity coordinates and visual perception (MacAdam ellipses [36–38]). In this paper, the viewing angle will be defined as the limit angle from which ΔE respect to normal incidence is larger than 2 in *Lab* space. For smaller angles, an incident angle-invariant substractive colors is considered. The viewing angles for the *on* state are 11.3°, 12.9° and 18.3° for cyan, magenta and yellow, respectively. Cyan and magenta present lower viewing angle than yellow. As previously stated, cyan and blue modes present smaller bandwidth because they are a consequence of second order resonances. The smaller the bandwidth, the stronger the effect of the blueshift on the reflected color. Blueshift is generated as a consequence of constructive interference condition. When incidence angle is increased, its cosine decreases, and therefore the wavelength λ decreases to keep the resonance condition.

This blueshift can be observed in Fig. 5(g). In the *off* mode, CMY colors show a viewing angle of around 36.5°. *Off* modes present higher viewing angle because, in general, their color coordinates do not depend on the resonant modes, and blueshift does not affect so much. In Fig. 5(h), the collection of colors for the different viewing angles is gathered in the chromaticity diagram. Arrows show the change in their coordinates as the angle of incidence is increased.

Optics EXPRESS

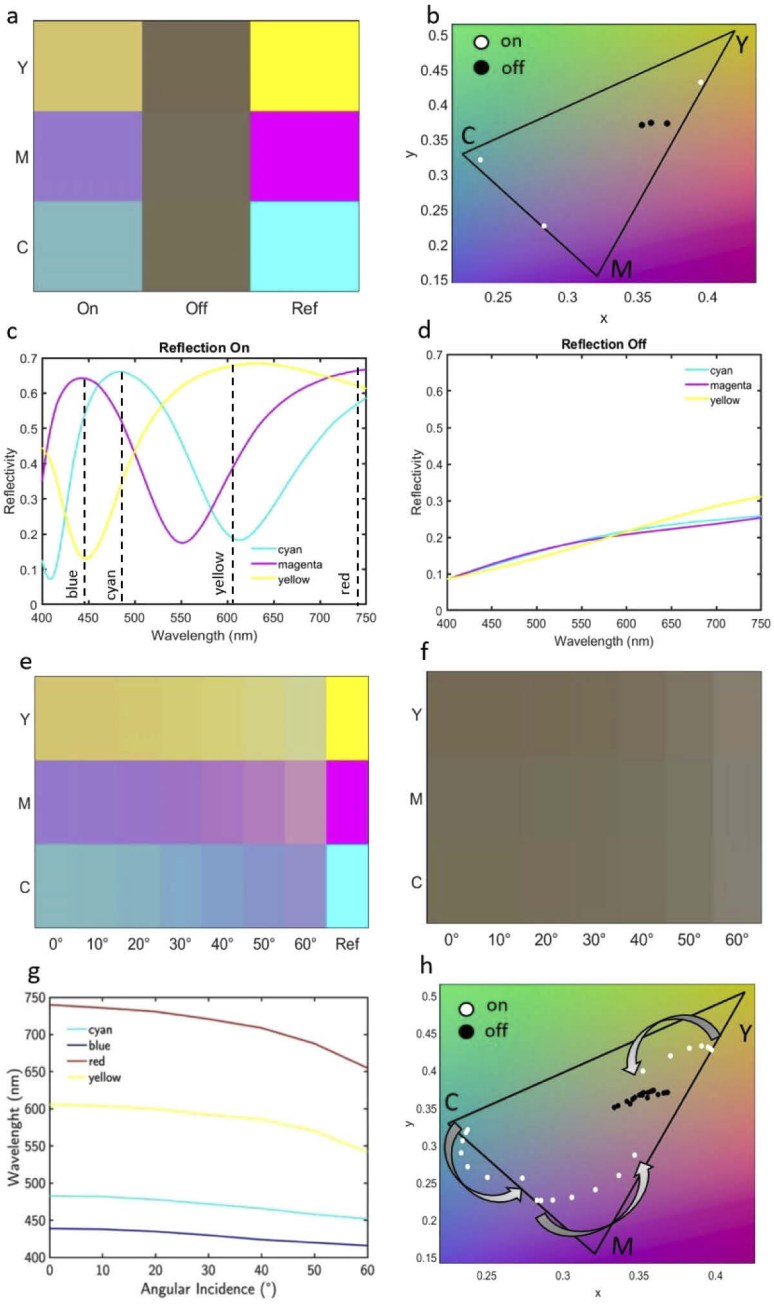

Fig. 5. (a) CMY colors generated by the reflective display for the *on* (left) and the *off* (center) modes compared to the standard CMY (right) as reference. (b) CMY colors generated by the reflective display for the *on* (white points) and *off* modes (black points) in the chromaticity diagram. Spectral reflectivity for optimized CMY in the *on* (c) and *off* (d) modes, respectively. Dashed lines indicates the wavelength at which cyan, blue, red and yellow resonant conditions hold. CMY color simulation for the *on* (e) and *off* modes (f) respectively and for different incident angles. (g) Cyan, blue, red and yellow resonant wavelengths as a function of the incident angle. (h) Resulting colors for the different viewing angles in the chromaticity diagram. Arrows show the change in their coordinates as the angle of incidence is increased.

Optics EXPRESS

4. Conclusions

We have designed a switchable on/off color reflective display made of AFPC based "pixels". An active layer of molybdenum oxide is introduced in the filter stack (ITO/MoO_x/ITO/Pt). Both modes can be generated due to the transition of MoO_x between a high absorbing medium and a transparent one when its oxygen content is increased from $x = 2$ to $x = 3$. This leads to the generation of proximate colors to standard CMY for the on mode and a constant pale color for the respective *off* state. To determine MoO_x and ITO thicknesses for this propose, an optimization algorithm has been created. This algorithm looks for an equilibrium between low ΔE respect CMY in the *on* mode and low ΔE between CMY *off* modes. This optimization is made for normal incidence, but AFPC reflectivity and the corresponding color, shows angular dependence. An angular study has been performed to simulate color for different incident angles. An Incident angle invariant substractive colors within the 0 to $\pm$ 11.3° has been obtained. In this range, reflected color remain constant and color difference cannot be appreciated by human perception.

Funding. This work has received funding from the European Union's Horizon 2020 research and innovation program under grant agreement (No 899598 – PHEMTRONICS).

Disclosures. The authors declare that there are no conflicts of interest related to this article.

Data availability. Data underlying the results presented in this paper are not publicly available at this time but may be obtained from the authors upon reasonable request.

References

1. C. H. Hare, "The degradation of coatings by ultraviolet light and electromagnetic radiation," J. Prot. Coat. Linings (1992).
2. T. Porwal, "Paint pollution harmful effects on environment," Int. J. Environ. Probl. **3**(9), 1–4 (2015).
3. S. Yokogawa, S. P. Burgos, and H. A. Atwater, "Plasmonic color filters for cmos image sensor applications," Nano Lett. **12**(8), 4349–4354 (2012).
4. Y.-W. Huang, W. T. Chen, W.-Y. Tsai, P. C. Wu, C.-M. Wang, G. Sun, and D. P. Tsai, "Aluminum plasmonic multicolor meta-hologram," Nano Lett. **15**(5), 3122–3127 (2015).
5. S. J. Tan, L. Zhang, D. Zhu, X. M. Goh, Y. M. Wang, K. Kumar, C.-W. Qiu, and J. K. Yang, "Plasmonic color palettes for photorealistic printing with aluminum nanostructures," Nano Lett. **14**(7), 4023–4029 (2014).
6. F. Cheng, J. Gao, L. Stan, D. Rosenmann, D. Czaplewski, and X. Yang, "Aluminum plasmonic metamaterials for structural color printing," Opt. Express **23**(11), 14552–14560 (2015).
7. X. M. Goh, Y. Zheng, S. J. Tan, L. Zhang, K. Kumar, C.-W. Qiu, and J. K. Yang, "Three-dimensional plasmonic stereoscopic prints in full colour," Nat. Commun. **5**(1), 5361–5368 (2014).
8. Y. Chen, X. Duan, M. Matuschek, Y. Zhou, F. Neubrech, H. Duan, and N. Liu, "Dynamic color displays using stepwise cavity resonators," Nano Lett. **17**(9), 5555–5560 (2017).
9. T. Xu, Y.-K. Wu, X. Luo, and L. J. Guo, "Plasmonic nanoresonators for high-resolution colour filtering and spectral imaging," Nat. Commun. **1**(1), 59 (2010).
10. T. D. James, P. Mulvaney, and A. Roberts, "The plasmonic pixel: large area, wide gamut color reproduction using aluminum nanostructures," Nano Lett. **16**(6), 3817–3823 (2016).
11. G. Si, Y. Zhao, J. Lv, M. Lu, F. Wang, H. Liu, N. Xiang, T. J. Huang, A. J. Danner, and J. Teng Liu, "Reflective plasmonic color filters based on lithographically patterned silver nanorod arrays," Nanoscale **5**(14), 6243–6248 (2013).
12. L. Shao, X. Zhuo, and J. Wang, "Advanced plasmonic materials for dynamic color display," Adv. Mater. **30**(16), 1704338 (2018).
13. J. Zheng, Z.-C. Ye, and Z.-M. Sheng, "Reflective low-sideband plasmonic structural colors," Opt. Mater. Express **6**(2), 381–387 (2016).
14. Y. Yu, L. Wen, S. Song, and Q. Chen, "Transmissive-reflective structural color filters: theory and applications," J. Nanomater. **2014**, 1–17 (2014).
15. S. D. Rezaei, R. J. Hong Ng, Z. Dong, J. Ho, E. H. Koay, S. Ramakrishna, and J. K. Yang, "Wide-gamut plasmonic color palettes with constant subwavelength resolution," ACS Nano **13**(3), 3580–3588 (2019).
16. K. Xiong, D. Tordera, M. P. Jonsson, and A. B. Dahlin, "Active control of plasmonic colors: emerging display technologies," Rep. Prog. Phys. **82**(2), 024501 (2019).
17. M. S. Rea, L. C. Radetsky, and J. D. Bullough, "Toward a model of outdoor lighting scene brightness," Light. Res. & Technol. **43**(1), 7–30 (2011).
18. C. Sung, J. Han, J. Song, C. S. Ah, S. M. Cho, and T.-Y. Kim, "Reflective-type transparent/colored mirror switchable device using reversible electrodeposition with fabry–perot interferometer," Adv. Mater. Technol. **5**(10), 2000367 (2020).

Optics EXPRESS

19. Z. Lin, Y. Long, X. Zhu, P. Dai, F. Liu, M. Zheng, Y. Zhou, and H. Duan, "Extending the color of ultra-thin gold films to blue region via fabry-pérot-cavity-resonance-enhanced reflection," Optik **178**, 992–998 (2019).
20. S. M. Cho, S. H. Cheon, T.-Y. Kim, C. S. Ah, J. Song, H. Ryu, and H. Y. Chu, "Design and fabrication of integrated fabry-perot type color reflector for reflective displays," J. Nanosci. Nanotechnol. **16**(5), 5038–5043 (2016).
21. Z. Yang, Y. Zhou, Y. Chen, Y. Wang, P. Dai, Z. Zhang, and H. Duan, "Reflective color filters and monolithic color printing based on asymmetric fabry–perot cavities using nickel as a broadband absorber," Adv. Opt. Mater. **4**(8), 1196–1202 (2016).
22. J. Zhao, M. Qiu, X. Yu, X. Yang, W. Jin, D. Lei, and Y. Yu, "Defining deep-subwavelength-resolution, wide-color-gamut, and large-viewing-angle flexible subtractive colors with an ultrathin asymmetric fabry–perot lossy cavity," Adv. Opt. Mater. **7**(23), 1900646 (2019).
23. M. Wuttig, H. Bhaskaran, and T. Taubner, "Phase-change materials for non-volatile photonic applications," Nat. Photonics **11**(8), 465–476 (2017).
24. P. Hosseini, C. D. Wright, and H. Bhaskaran, "An optoelectronic framework enabled by low-dimensional phase-change films," Nature **511**(7508), 206–211 (2014).
25. C. Ríos, P. Hosseini, R. A. Taylor, and H. Bhaskaran, "Color depth modulation and resolution in phase-change material nanodisplays," Adv. Mater. **28**(23), 4720–4726 (2016).
26. P. Hosseini and H. Bhaskaran, "Colour performance and stack optimisation in phase change material based nano-displays," in *Integrated Photonics: Materials, Devices, and Applications III*, vol. 9520 (International Society for Optics and Photonics, 2015), p. 95200M.
27. C. Talagrand, G. Triggs, L. Bandhu, S. Garcia-Castillo, B. Broughton, H. Bhaskaran, and P. Hosseini, "Solid-state reflective displays (srd®) for video-rate, full color, outdoor readable displays," J. Soc. Inf. Disp. **26**(10), 619–624 (2018).
28. C. Talagrand, L. Bandhu, P. Hosseini, H. Bhaskaran, B. Broughton, S. Garcia-Castillo, and M. Yang, "Solid-state reflective displays (srd) utilizing ultrathin phase-change materials," in *SID Symposium Digest of Technical Papers*, vol. 48 (Wiley, 2017).
29. S. G.-C. Carrillo, L. Trimby, Y.-Y. Au, V. K. Nagareddy, G. Rodriguez-Hernandez, P. Hosseini, C. Ríos, H. Bhaskaran, and C. D. Wright, "A nonvolatile phase-change metamaterial color display," Adv. Opt. Mater. **7**(18), 1801782 (2019).
30. D. O. Scanlon, G. W. Watson, D. Payne, G. Atkinson, R. Egdell, and D. Law, "Theoretical and experimental study of the electronic structures of moo3 and moo2," J. Phys. Chem. C **114**(10), 4636–4645 (2010).
31. X. Duan, S. T. White, Y. Cui, F. Neubrech, Y. Gao, R. F. Haglund, and N. Liu, "Reconfigurable Multistate Optical Systems Enabled by VO 2 Phase Transitions," ACS Photonics **7**(11), 2958–2965 (2020).
32. Q. Zhang, X. Li, Q. Ma, Q. Zhang, H. Bai, W. Yi, J. Liu, J. Han, and G. Xi, "A metallic molybdenum dioxide with high stability for surface enhanced raman spectroscopy," Nat. Commun. **8**(1), 14903 (2017).
33. Y. Gutiérrez, A. S. Brown, F. Moreno, and M. Losurdo, "Plasmonics beyond noble metals: Exploiting phase and compositional changes for manipulating plasmonic performance," J. Appl. Phys. **128**(8), 080901 (2020).
34. H. A. Macleod, *Thin-film optical filters* (CRC, 2017), chap. 2.
35. Z. H. Mohammed, "The fresnel coefficient of thin film multilayer using transfer matrix method tmm," in *IOP Conference Series: Materials Science and Engineering*, vol. 518 (IOP Publishing, 2019), p. 032026.
36. P. Capilla and J. Pujol, *Fundamentos de colorimetría* (Universitat de València, 2002), chap. 1.
37. D. Malacara, *Color vision and colorimetry: Theory and applications* (SPIE-The International Society for Optical Engineering, 2002), chap. 2.
38. W. Mokrzycki and M. Tatol, "Colour difference delta e-a survey," Mach. Graph. Vis **20**, 383–411 (2011).